

# Prediction of the vibro-acoustic response of a structure-liner-fluid system based on a patch transfer function approach and direct experimental subsystem characterisation

Christopher G. Albert<sup>a,b,\*</sup>, Giorgio Veronesi<sup>a</sup>, Eugène Nijman<sup>a</sup>, Jan Rejlek<sup>a</sup>

<sup>a</sup>*Virtual Vehicle Research Center, Inffeldgasse 21A, A-8010 Graz, Austria*

<sup>b</sup>*Institut für Theoretische Physik – Computational Physics,  
Technische Universität Graz, Petersgasse 16, A-8010 Graz, Austria*

---

## Abstract

The vibro-acoustic response of a structure-liner-fluid system is predicted by application of a patch transfer function (PTF) coupling scheme. In contrast to existing numerical approaches, PTF matrices of structure and liner are determined by a direct experimental approach, avoiding the requirement of material parameters. Emphasis is placed on poroelastic lining materials. The method accounts for surface input and next-neighbour transfer terms and for cross and cross-transfer terms through the specimen. Shear stresses and transfer terms to further patches on the liner are neglected. A single test-rig characterisation procedure for layered poroelastic media is proposed. The specimen is considered as a single component – no separation of layers is performed. For this reason the characterisation procedure can serve as a complement to existing methods if separation of layers is not possible and as a tool for validation of more detailed material models. Problem specific boundary conditions for skeleton and fluid, which may cause non-reciprocal cross terms, are dealt with by the procedure. Methods of measurement for the assessment of PTF matrices are presented and their accuracy and limitations are discussed. An air gap correction method for surface impedance measurements is presented.

**Keywords:** Vibro-acoustic coupling, Impedance matrix, Patch transfer functions, Poroelastic material, *PU*-probes

---

## 1. Introduction

Poroelastic lining materials are widely applied as dissipative treatments in vibro-acoustic systems. When a structure is radiating into a cavity, the insertion of poroelastic damping layers has three main effects: Structural loading and damping, decoupling the cavity from the structure (mass-spring systems) and adding absorption to the cavity.

---

\*Corresp. author. Tel.: +43 3168738174; fax: +43 3168738677

Email address: albert@alumni.tugraz.at (Christopher G. Albert)

Preprint submitted to Elsevier

21st July 2016

In traditional numerical simulations [1], the influence on the structure is usually described by additional mass and damping. The damping imposed on the cavity by the poroelastic layer is captured by an impedance boundary condition in the simplest case. Required parameters may be estimated by material models, ranging from simple equivalent mechanical systems to phenomenological impedance models (e.g. [2]). Mechanical parameters of lining materials may be obtained in dynamic stiffness tests and impedances are measured in a standing wave tube or in situ on the material surface [3]. Depending on the type of lining material and the desired accuracy, more detailed models are required. A common approach is based on the Biot model for poroelasticity in a full FEM simulation [4] or in a reduced transfer matrix scheme [5]. Material parameters, such as porosity or flow resistivity can be obtained experimentally on material samples. Due to the variety of material properties (e.g. viscoelastic skeleton, anisotropy, etc.), modelling and characterisation of poroelastic material are an area of active research [6].

The patch transfer function (PTF) coupling scheme [7, 8, 9] has been introduced as a method to reduce the calculation time in coupled fluid/fluid and fluid/structure simulations. While having been developed for numerical applications, the relatively small number of discrete surface elements (patches) makes this approach also applicable to experimental characterisation of physical systems [10, 11]. For structure-borne sound similar approaches have been introduced to couple subsystems by mobility matrices (e.g. [12]).

In this article the PTF methodology is applied to a physical structure/liner/fluid system with experimentally characterised structure and liner. The principles of the coupling method and the experimental realisation for the subsystem characterisation are presented. Particular emphasis is given to the liner characterisation method, which is non-destructive and can be performed on flat and isotropic samples. Non-local effects due to wave propagation in the lateral direction of the liner are accounted for by transfer terms. Propagation across the thickness of the material is described by cross terms. Mechanical separation of the layers, with the risk of modifying their characteristics, is not necessary.

The described direct characterisation methods are intended to capture the response of a subsystem as-is. For example if no reliable numerical models are available for a complex structure such as a car body, experimentally acquired patch mobilities may be used instead. A direct experimental liner characterisation may not only be of interest when no material models are available, but also for materials where a separation of layers is not possible or when parameters vary continuously across the sample thickness. However, results from a direct experimental characterisation do not allow for later adjustments in material parameters or geometry. For these reasons, the approach is considered as *complementary to* rather than as a *replacement for* micro-models based on material parameters. Since patch transfer matrices can also be computed from the latter, the proposed methods might be useful as an intermediate-step experimental verification of modelling results.

Characterisation results of isolated subsystems and the coupled system are presented in section 4. An overview of the limitations of PTF coupling and characterisation methods can be found in section 6. The range of validity is roughly set by the frequency where the wavelength in any of the coupled systems reaches the spatial aliasing limit. High dynamic range of sensors and highly accurate calibration and characterisation measurements are required to avoid random and systematic errors masking the results.

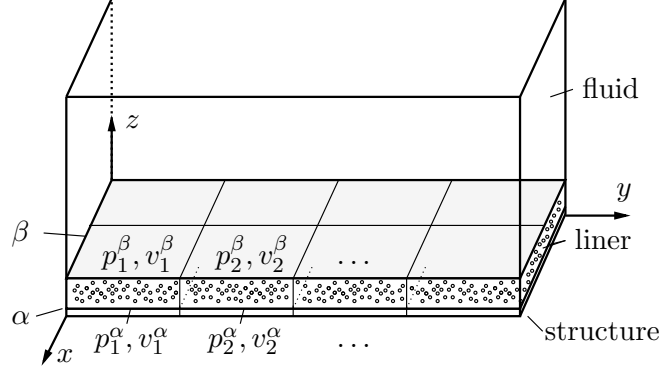


Figure 1: Coupled system discretised into patches. The  $\alpha$  and  $\beta$  superscripts indicate the structure/liner interface and the liner/fluid interface respectively.

## 2. Theory

### 2.1. Patch transfer functions

This section introduces PTF coupling equations for a built-up system consisting of a structure, liner and fluid domain. The system is discretised by a patch grid as shown in Figure 1. The arithmetic mean of complex field amplitudes is taken over each patch surface. Thereby, integral equations for infinitesimal elements and Green's functions are approximated by matrix equations for discrete patches. Detailed derivations of the patch transfer function method can be found in [7, 9, 13]. The present approach considers only out-of-plane velocities for the coupling procedure without explicitly including shear stresses when coupling to the liner. This is justified at least in the case of a thin plate-like structure, where in-plane and out-of-plane velocity are directly related and the directivity of the radiated wave is similar with and without liner [5]. If there is no direct contact between structure and liner (a thin layer of air in-between) it is also possible to neglect shear stresses [14].

In the following a slightly alternative matrix formulation is used to describe coupling between sub-systems. Structure and fluid are, as usual, characterised by respectively a mobility matrix  $\mathbf{Y}$  and an impedance matrix  $\mathbf{Z}$ . Since patch-averaged pressures  $p_i$  and velocities  $v_i$  are the governing variables, an impedance or mobility term can be either interpreted as a patch-averaged acoustic surface impedance/mobility or a mechanical impedance  $Z_{\text{mech}}/S_p$  or mobility  $S_p Y_{\text{mech}}$  normalised by a factor of the patch area  $S_p$ . The liner will be characterised by a hybrid matrix  $\mathbf{H}$  instead of a conventional impedance matrix. A similar technique has been described by Atalla et al. [4] to integrate poroelastic materials into finite element models of structural and acoustic domains.

The interface between the liner and the structure (respectively the cavity) is referred to as face  $\alpha$  (respectively face  $\beta$ , see Figure 1). Positive velocities are directed upwards by convention, which leads to a change of signs in the mobility relation of the structure. The velocity response of the structure due to a pressure excitation on face  $\alpha$  is given by

$$\mathbf{v}^\alpha = -\mathbf{Y}\mathbf{p}^\alpha. \quad (1)$$

The mobility  $\mathbf{Y}$  is an intrinsic property of the structure, so relation (1) holds independently from the actual source of the pressure – whether it is due to an external excitation or due to the coupled response of another subsystem. If an excitation of  $p_n^\alpha = 1$  at position  $n$  of an otherwise free ( $p_{m \neq n}^\alpha = 0$ ) structure is applied, the resulting response velocities are the elements of the  $n$ -th row of  $\mathbf{Y}$ .

The fluid surface impedance on  $\beta$  relates pressures and velocities on the upper liner-fluid coupling surface,

$$\mathbf{p}^\beta = \mathbf{Z}\mathbf{v}^\beta. \quad (2)$$

This relation is again independent of the coupling and the  $n$ -th row of  $\mathbf{Z}$  is equal to the hypothetically blocked ( $v_{n \neq m}^\beta = 0$ ) pressures due to an excitation of  $v_n^\beta = 1$  at position  $n$ .

A relationship between pressure and velocity on the two surfaces of the liner is given by the matrix equation

$$\begin{bmatrix} \mathbf{p}^\alpha \\ \mathbf{v}^\beta \end{bmatrix} = \mathbf{H} \begin{bmatrix} \mathbf{v}^\alpha \\ \mathbf{p}^\beta \end{bmatrix} = \begin{bmatrix} \mathbf{h}^{\alpha\alpha} & \mathbf{h}^{\alpha\beta} \\ \mathbf{h}^{\beta\alpha} & \mathbf{h}^{\beta\beta} \end{bmatrix} \begin{bmatrix} \mathbf{v}^\alpha \\ \mathbf{p}^\beta \end{bmatrix}. \quad (3)$$

$\mathbf{v}^\alpha$  describes a velocity (kinematic) excitation from the bottom side and  $\mathbf{p}^\beta$  a pressure excitation from the top side.

For the one-dimensional case (one patch on each side), bottom and top quantities  $\mathbf{p}^i$ ,  $\mathbf{v}^i$  and sub-matrices  $\mathbf{h}^{ij}$  are given by scalars  $p^i$ ,  $v^i$ ,  $h^{ij}$  that may be interpreted in the following way:

$$h^{\alpha\alpha} = \left. \frac{p^\alpha}{v^\alpha} \right|_{p^\beta=0} \quad (4)$$

is the impedance as seen from the bottom side while keeping the top side free (the inverse of the bottom mobility).

$$h^{\alpha\beta} = \left. \frac{p^\alpha}{p^\beta} \right|_{v^\alpha=0} \quad (5)$$

is the transmission ratio from a pressure excitation on the top to the blocked bottom.

$$h^{\beta\alpha} = \left. \frac{v^\beta}{v^\alpha} \right|_{p^\beta=0} \quad (6)$$

is the transmission ratio from a velocity excitation on the bottom to the free top.

$$h^{\beta\beta} = \left. \frac{v^\beta}{p^\beta} \right|_{v^\alpha=0} \quad (7)$$

is the top surface mobility (the inverse of the surface impedance) with a blocked bottom.

The  $\mathbf{H}$ -matrix elements can in principle be obtained by straightforward measurement of the state variables, provided well defined boundary conditions are imposed. As will become clear in section 3.3 it is actually not necessary to measure the matrix elements under idealised conditions (velocity blocked at the bottom interface, pressure release at the top interface), but rather reconstruct them by solving an inverse problem for conditions similar to the ideal case.

Let  $\tilde{\mathbf{v}}^\alpha$  and  $\tilde{\mathbf{p}}^\alpha$  be the source terms, i.e. the responses of the isolated systems without liner to *internal* excitations (not on  $\alpha$  or  $\beta$ ). In other words,  $\tilde{\mathbf{v}}^\alpha$  is the response of the free ( $\tilde{\mathbf{p}}^\alpha = \mathbf{0}$ ) structure due to some internal structural excitation and  $\tilde{\mathbf{p}}^\beta$  the response of the blocked ( $\tilde{\mathbf{v}}^\beta = \mathbf{0}$ ) fluid due to some internal acoustical excitation. Then, using the superposition principle [13], the response of the coupled system is given by the following set of equations:

$$\mathbf{v}^\alpha = \tilde{\mathbf{v}}^\alpha - \mathbf{Y}\mathbf{p}^\alpha, \quad (8)$$

$$\mathbf{p}^\alpha = \mathbf{h}^{\alpha\alpha}\mathbf{v}^\alpha + \mathbf{h}^{\alpha\beta}\mathbf{p}^\beta, \quad (9)$$

$$\mathbf{v}^\beta = \mathbf{h}^{\beta\alpha}\mathbf{v}^\alpha + \mathbf{h}^{\beta\beta}\mathbf{p}^\beta, \quad (10)$$

$$\mathbf{p}^\beta = \tilde{\mathbf{p}}^\beta + \mathbf{Z}\mathbf{v}^\beta, \quad (11)$$

or in matrix form

$$\begin{bmatrix} \mathbf{I} & \mathbf{Y} & 0 & 0 \\ -\mathbf{h}^{\alpha\alpha} & \mathbf{I} & 0 & -\mathbf{h}^{\alpha\beta} \\ -\mathbf{h}^{\beta\alpha} & 0 & \mathbf{I} & -\mathbf{h}^{\beta\beta} \\ 0 & 0 & -\mathbf{Z} & \mathbf{I} \end{bmatrix} \begin{bmatrix} \mathbf{v}^\alpha \\ \mathbf{p}^\alpha \\ \mathbf{v}^\beta \\ \mathbf{p}^\beta \end{bmatrix} = \begin{bmatrix} \tilde{\mathbf{v}}^\alpha \\ 0 \\ 0 \\ \tilde{\mathbf{p}}^\beta \end{bmatrix}. \quad (12)$$

For the case without liner where surfaces  $\alpha$  and  $\beta$  coincide, the corresponding reduced  $\mathbf{H}$ -matrix is given by

$$\mathbf{H} = \begin{bmatrix} \mathbf{0} & \mathbf{I} \\ \mathbf{I} & \mathbf{0} \end{bmatrix} \quad (13)$$

and (12) is reduced to

$$\begin{bmatrix} \mathbf{I} & \mathbf{Y} \\ -\mathbf{Z} & \mathbf{I} \end{bmatrix} \begin{bmatrix} \mathbf{v} \\ \mathbf{p} \end{bmatrix} = \begin{bmatrix} \tilde{\mathbf{v}} \\ \tilde{\mathbf{p}} \end{bmatrix}, \quad (14)$$

where  $\mathbf{v}^\alpha = \mathbf{v}^\beta = \mathbf{v}$  and  $\mathbf{p}^\alpha = \mathbf{p}^\beta = \mathbf{p}$ .

### 3. Subsystem characterisation

$\mathbf{Y}$ ,  $\mathbf{Z}$  and  $\mathbf{H}$  may be obtained by either numerical or experimental means. In existing works, PTF matrices were derived by analytical [7, 9] or numerical [8] means. In the following sections some techniques for the direct experimental characterisation of subsystems without the requirement of a material numerical model are proposed. In the reconstruction these subsystems are combined with each other or with their numerical counterparts to predict the response of the coupled system.

The principle of the proposed characterisation method consists in the measurement of the isolated subsystem response for a number of load cases equal to the number of

patches, thereby forming a full set of linear equations. The effort required for the experimental characterisation of a subsystem scales with the square of the number of surface patches, since the transfer function is measured between each pair of patches. The required time to characterise a grid of 32 patches on a structure is in the order of 2-3 working days. The characterisation of the next-neighbour  $\mathbf{H}$ -matrix of a liner specimen is usually performed within half a working day. For fluid cavities, no reliable data is available yet.

### 3.1. Structure

A structure with a relatively high impedance is assumed to be freely vibrating in air ( $Y^{-1} \gg Z_0$ ). Therefore, it is possible to measure the terms  $y_{ij}$  of the mobility matrix in a direct way by exciting on position  $j$  and measuring the velocity on position  $i$ . In our case the excitation was applied by means of an impact hammer. An excitation similar to a uniform pressure excitation was realised by averaging over a sufficient number of hammer blows on an equidistant grid inside a patch. If the grid point distance is small compared to the structural wavelength, the excitation corresponds to a uniform pressure excitation of the whole patch. Convergence to this condition can be proven theoretically by wavelength criteria and experimentally by reaching the level of grid refinement where the results stop changing significantly in the desired frequency range. The response can be measured, as in our case, by a grid of accelerometers, a scanning laser vibrometer or by an array of  $PU$ -probes. In practice, convergence was reached by a  $4 \times 4$  grid of excitation and receiver positions per patch for the plate described in section 4.1, which has been confirmed by a Kirchhoff-Love model.

### 3.2. Fluid

A realisation of an experimental cavity characterisation is currently under investigation but has not been performed yet. For a direct characterisation of the fluid cavity a flat, square-shaped piston source should in principle be progressively positioned in the different patch locations. As an alternative to this piston-like radiator, a superposition of excitations by a point source ("tube" source) might be possible, analogous to the point excitation of the structure with a hammer. The blocked (the cavity must be equipped with a high impedance wall) pressure response  $z_{ij}$  would be measured using an array of pressure microphones or  $PU$ -probes, where  $PU$ -probes offer the advantage of directly measuring the particle velocity on the exciting patch.

### 3.3. Liner characterisation – fundamentals

Acoustical liners feature a porous solid phase (also referred to as skeleton or matrix) with interconnected interstitial cavities filled with a fluid phase (air). At the two coupling surfaces the area fraction occupied by the solid phase is very small. At the structure/liner interface, however, the considerable pressure concentrations in the tiny contact areas between skeleton and adjacent structure cause fluid and skeleton to have the same normal velocity. The characterisation procedure must account for this feature and mechanical excitation with a piston is thus necessary at this interface in order to obtain representative data.

Moreover, at the structure/liner interface both solid as well as fluid phase may significantly contribute to the average patch pressure, and microphones can consequently not

be used, but the average patch pressure must be obtained indirectly through piston force measurements.

At the liner/fluid interface, on the other hand, the fluid of the cavity adjacent to the liner is unable to support shear stresses and no pressure concentration will occur. Usually continuity of pressure, normal stresses and normal displacements are assumed on the liner/fluid interface [15]. In the coupling conditions, displacements of fluid and solid phase of the poroelastic material are weighted depending on its porosity. Consequently, normal velocities of fluid and solid phase do not necessarily coincide, as opposed to the structure/liner interface. The characterisation procedure should therefore use an acoustic excitation together with microphones and particle velocity sensors at the liner/fluid interface, while avoiding a direct mechanical excitation there which would kinematically couple normal displacements of solid and fluid phase.

To experimentally re-construct the  $\mathbf{H}$  matrix on the  $2N$  patches (top and bottom),  $2N$  linearly independent load cases are needed while measuring pressure and velocity on all patches. These load cases are imposed by structural shaker excitations on the lower surface  $\alpha$  and speaker excitations on the upper surface  $\beta$ . The measurement of pressures and velocities on top and bottom side is performed by a combination of force transducers, accelerometers on the bottom side and *PU*-probes on the top side. In principle one shaker and one speaker is needed for each patch excitation. A sketch of the test rig is displayed in Figure 2. Stable results for two patches were obtained using the following four excitation conditions as a sweep or noise signals in the considered frequency range:

- I* : loudspeakers “off” and shaker A “on”,
- II* : loudspeakers “off” and shaker B “on”,
- III* : shakers “off” and speakers A and B “on” in phase,
- IV* : shakers “off” and speakers A and B “on” in anti-phase.

For the air gap correction (section 3.5) load cases *III* and *IV* are applied once more with the liner specimen replaced by a rigid dummy.

### 3.3.1. Bottom surface active patch

The bottom surface of the liner is excited by a shaker on patch  $i$ . To excite the whole patch, a patch-sized lightweight piston is mounted on top of the shaker. The velocity of the piston,  $v_i^\alpha$ , is measured using an accelerometer. Since a direct pressure measurement on the interface between piston and liner is difficult to achieve, the reaction force  $F_i^{\alpha, \text{meas}}$  below the piston is measured instead by force cells. This force includes the response of both piston and liner. In the frequency range, where the piston moves as a rigid body, the reaction pressure on the liner bottom surface is given by

$$p_i^\alpha = F_i^{\alpha, \text{meas}}/S_p - Z_i^{\text{act}}v_i^\alpha, \quad (15)$$

where  $Z_i^{\text{act}}$  is the piston’s acoustic impedance and  $S_p$  is the area of one patch.

For a rigid piston,

$$Z_i^{\text{act}} = Z_{\text{m}, i}^{\text{act}} + Z_{\text{rad}, i}^{\text{act}} \quad (16)$$

is governed by a mass-like mechanical impedance normalised to the patch area,  $Z_{\text{m}, i}^{\text{act}} = i\omega m_i/S_p$  and the acoustic radiation impedance  $Z_{\text{rad}, i}^{\text{act}}$ . It is determined by a calibration measurement consisting of driving the plate without liner. Like in the later characterisation measurement, the force  $F_i^{\alpha, \text{cal}}$  below the piston is measured by the force transducers and the pressure  $p_i^{\alpha, \text{cal}}$  flush to the piston surface as well as the piston velocity

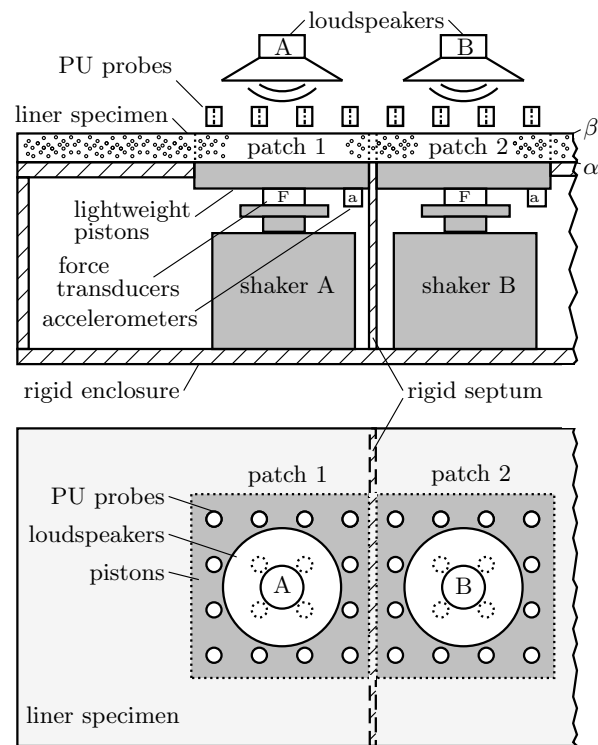


Figure 2: Liner test rig for two patches in cross-sectional view (top) and from above (bottom). Load cases are imposed by loudspeakers A, B and shakers A, B via square pistons. The response is measured by PU probes, accelerometers and force transducers. Enclosure and septum avoid acoustic leakage and the latter is thin compared to the patch width.



$v_i^{\alpha, \text{cal}}$  using a *PU*-probe array. The *PU* particle velocity sensor sensitivities are adjusted to match the piston accelerometer reading. The piston's acoustical impedance on patch  $i$  is obtained as

$$Z_i^{\text{act}} = \frac{F_i^{\alpha, \text{cal}}/S_p - p_i^{\alpha, \text{cal}}}{v_i^{\alpha, \text{cal}}}. \quad (17)$$

### 3.3.2. Bottom surface passive patches

For load cases requiring a non-driven bottom patch  $j$ , the pressure on the plate surface is determined indirectly by the relation

$$p_j^{\alpha} = Z_j^{\text{pass}} v_j^{\alpha}. \quad (18)$$

Here the acoustical impedance  $Z_j^{\text{pass}}$  of the passive plate is again obtained through a calibration measurement. The speaker on patch  $j$  is switched on and the calibration pressure  $p_j^{\alpha, \text{cal}}$  is again determined from measurements with the *PU* array flush to the surface. The impedance of the passive system (combination of plate and remaining set-up below) is then given directly as

$$Z_j^{\text{pass}} = \frac{p_j^{\alpha, \text{cal}}}{v_j^{\alpha, \text{cal}}}. \quad (19)$$

### 3.3.3. Top surface

Acoustical excitation is provided by loudspeakers centred above each patch as shown in Figure 2. Pressures and velocities are measured by averaging over an array of *PU*-probes located between the loudspeaker and the liner as close as possible to the surface of the latter.

### 3.3.4. Reconstruction of the *H*-matrix

According to (3), the **H**-matrix of the liner can be reconstructed from  $2N$  load cases by

$$\mathbf{H} = \begin{bmatrix} \mathbf{P}^{\alpha} \\ \mathbf{V}^{\beta} \end{bmatrix} \begin{bmatrix} \mathbf{V}^{\alpha} \\ \mathbf{P}^{\beta} \end{bmatrix}^{-1}, \quad (20)$$

where the matrices  $\mathbf{P}^{\alpha}$ ,  $\mathbf{P}^{\beta}$ ,  $\mathbf{V}^{\alpha}$ ,  $\mathbf{V}^{\beta}$  contain the excitation and response pressures and velocities for each load case (labelled by Roman numerals  $I, II, \dots$ ) in one column, i.e.

$$\begin{bmatrix} \mathbf{V}^{\alpha} \\ \mathbf{P}^{\beta} \end{bmatrix} = \begin{bmatrix} \mathbf{v}^{\alpha} \\ \mathbf{p}^{\beta} \end{bmatrix}_I \begin{bmatrix} \mathbf{v}^{\alpha} \\ \mathbf{p}^{\beta} \end{bmatrix}_{II} \cdots \begin{bmatrix} \mathbf{v}^{\alpha} \\ \mathbf{p}^{\beta} \end{bmatrix}_{2N}. \quad (21)$$

In principle any linearly independent set of excitation conditions is suited to reconstruct the matrix **H**. In practice, however, bad conditioning of the matrix  $\begin{bmatrix} \mathbf{V}^{\alpha} \\ \mathbf{P}^{\beta} \end{bmatrix}$  may lead to substantial error amplification in the inversion process, especially when experimental data containing inevitable inaccuracies have to be processed. Ideal excitation conditions consist of an orthonormal set of vectors  $\begin{bmatrix} \mathbf{v}^{\alpha} \\ \mathbf{p}^{\beta} \end{bmatrix}_i$ . In the following section a simplification will be introduced to reduce the number of load cases using symmetry properties.

### 3.4. Liner characterisation – further remarks

#### 3.4.1. Decay and Symmetries

Wave propagation inside the liner in the lateral (in-plane) direction is characterised by spatial decay. In the particular case of a moulded foam with a limp heavy layer considered in this article only the driven patch itself and the patch adjacent to the driven patch need to be considered, whereas propagation to farther patches can be neglected. Such an assumption can be checked in the following ways.

When approximate values of material data such as stiffness or damping are known, transfer matrix terms to further patches can be estimated from a corresponding material model. In the particular case considered in this article, a numerical model of an equivalent elastic material has been constructed and updated using the characterisation results. Another option consists in measuring further transfer terms by adjustable patch positions in the test rig. Once the additional terms do not change the reconstruction significantly, the remaining transfer functions to further patches are not characterised and set to zero in the calculation.

$\mathbf{H}$  may consequently be approximated by a banded matrix and the test rig be limited to two patches in the present case. For two adjacent patches 1 and 2, pressures and velocities are labelled  $p_1^i, p_2^i, v_1^i$  and  $v_2^i$ . The elements of the  $2 \times 2$  sub-matrices of a banded  $\mathbf{H}$  matrix in equation (3) are

$$h_{(12)}^{ij} = \begin{bmatrix} h_{11}^{ij} & h_{12}^{ij} \\ h_{21}^{ij} & h_{22}^{ij} \end{bmatrix}, \quad (22)$$

with surface  $i, j \in \{\alpha, \beta\}$ . If the material is both homogeneous and isotropic in the lateral direction, the corresponding sub-matrices  $h_{(ab)}^{ij}$  for any two adjacent patches  $a$  and  $b$  are identical and symmetric. The single elements of  $h_{(ab)}^{ij} = h_{(12)}^{ij} =: h^{ij}$  are called input (in) and transfer (tr) terms, where

$$h^{ij} = \begin{bmatrix} h_{\text{in}}^{ij} & h_{\text{tr}}^{ij} \\ h_{\text{tr}}^{ij} & h_{\text{in}}^{ij} \end{bmatrix}. \quad (23)$$

The input element  $h_{\text{in}}^{ij} = h_{11}^{ij} = h_{22}^{ij}$  describes the input response and the transfer element  $h_{\text{tr}}^{ij} = h_{12}^{ij} = h_{21}^{ij}$  the response of the next neighbour.

This symmetry leads to a reduction of the required load cases in the characterisation measurements. Let  $I$  denote a load case where an excitation of  $v_1^\alpha$  is applied on patch 1 and  $v_2^\alpha$  on patch 2. In load case  $II$  identical excitations are applied but the patches are swapped, so  $v_2^\alpha$  is applied on patch 1 and  $v_1^\alpha$  on patch 2. Making use of the symmetry properties of  $h^{ij}$ , one can identify

$$\begin{aligned} \begin{bmatrix} p_1^\alpha \\ p_2^\alpha \end{bmatrix}_{II} &= \begin{bmatrix} h_{\text{in}}^{\alpha\alpha} & h_{\text{tr}}^{\alpha\alpha} \\ h_{\text{tr}}^{\alpha\alpha} & h_{\text{in}}^{\alpha\alpha} \end{bmatrix} \begin{bmatrix} v_1^\alpha \\ v_2^\alpha \end{bmatrix}_{II} + \dots \\ &= \begin{bmatrix} h_{\text{in}}^{\alpha\alpha} & h_{\text{tr}}^{\alpha\alpha} \\ h_{\text{tr}}^{\alpha\alpha} & h_{\text{in}}^{\alpha\alpha} \end{bmatrix} \begin{bmatrix} v_2^\alpha \\ v_1^\alpha \end{bmatrix}_I + \dots = \begin{bmatrix} p_2^\alpha \\ p_1^\alpha \end{bmatrix}_I. \end{aligned} \quad (24)$$

Similar identities hold for the remaining possible excitation and response quantities, which leads to a reduction of the required load cases by half. The remaining (virtual)

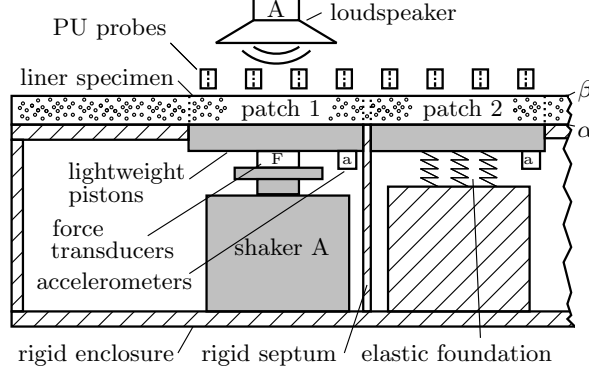


Figure 3: Reduced liner test rig with one active patch excited by a shaker and one passive patch with an elastic foundation.

load cases are introduced by swapping patch indices. This leads to the possibility of a reduced version of the test rig with excitation only on patch 1 (Figure 3). In this set-up the piston below patch 2 is bedded on an elastic foundation (e.g. springs or elastic foam). The pressure response below patch 2 is measured indirectly by the piston velocity as described in subsection 3.3.2. The bedding should be chosen such that translational and rotational mass-spring resonances are well below the measurement range.

#### 3.4.2. Uncertainties in the indirect measurements

It has to be noted that  $Z_i^{\text{act}}$  in (15) is not necessarily the actual impedance of the free plate, but rather a calibration factor that compensates for the combination of the plate impedance and the calibration between force cell and microphones. From equation (15), the uncertainty  $\Delta p_i^\alpha$  of the liner reaction pressure on the active patch  $i$  due to the uncertainty  $\Delta F_i^{\alpha, \text{meas}}$  of the measured force  $F_i^{\alpha, \text{meas}}$  is

$$\begin{aligned} \Delta p_i^\alpha &= \Delta F_i^{\alpha, \text{meas}} / S_p \\ &= \frac{\Delta F_i^{\alpha, \text{meas}}}{F_i^{\alpha, \text{meas}}} \frac{F_i^{\alpha, \text{meas}}}{S_p} \\ &= \frac{\Delta F_i^{\alpha, \text{meas}}}{F_i^{\alpha, \text{meas}}} (p_i^\alpha + Z_i^{\text{act}} v_i^\alpha). \end{aligned} \quad (25)$$

For nearly blocked bottom and nearly open top, one can assume

$$p_i^\alpha \approx h_{\text{in}}^{\alpha\alpha} v_i^\alpha. \quad (26)$$

Using this relation in (25) leads to an estimate of the absolute error of

$$\Delta p_i^\alpha \approx \frac{\Delta F_i^{\alpha, \text{meas}}}{F_i^{\alpha, \text{meas}}} \left( 1 + \frac{Z_i^{\text{act}}}{h_{\text{in}}^{\alpha\alpha}} \right) p_i^\alpha.$$

The relative error in the reconstructed liner pressure is thus amplified as compared to the relative error in the direct force measurements. The amplification factor is governed

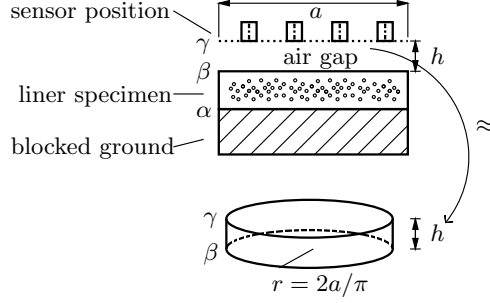


Figure 4: Air gap of height  $h$  and equivalent air cylinder.

by the ratio of piston and liner input impedance and thus, to a large extent, by the piston mass. The piston must consequently not only behave like a rigid body in the frequency range of interest but also be as lightweight as possible in order to minimise the measurement uncertainty.

For the measurement on a passive plate  $j$ , a lightweight plate ensures a higher velocity signal

$$v_j^\alpha \approx \frac{h_{tr}^{\alpha\alpha}}{Z_j^{\text{pass}}} \quad (27)$$

above the noise level.

### 3.5. Air gap correction

In principle the *PU*-probes should be located in correspondence with the top surface of the liner ( $\beta$ -surface), but in practice a slight air gap between the liner surface and the plane of the transducers is unavoidable. This air gap results in two error sources. On one hand the air layer may exhibit radiation through the side walls of the gap, on the other hand, the stiffness of the layer itself is finite.

The correction that will be applied for the rectangular patches is based on a direct experimental characterisation of the air gap that will be described in the following subsection. The qualitative behaviour of the air gap can be illustrated by considering a thin cylindrical air gap (Figure 4) of the same circumference as a patch.

To estimate the acoustic input impedance  $Z_{\text{gap}}$  of the air gap, the sample in the figure is replaced by a rigid surface. In the frequency range where the wavelength is small in comparison to the patch dimension,  $Z_{\text{gap}}$  is composed of the stiffness of the air volume  $V = \pi r^2 h$  with bulk modulus  $K_{\text{air}}$  coupled in series to a radiation impedance  $Z_{\text{rad}}$  at the outer rim. A uniform velocity excitation  $v^\gamma$  at the upper boundary  $\gamma$  of the air gap leads to a compression of

$$\Delta V = \pi r^2 \Delta h = \pi r^2 \frac{v^\gamma}{i\omega}, \quad (28)$$

so

$$Z_{\text{gap}} = \frac{p^\gamma}{v^\gamma} = \frac{r}{2h} \left( \frac{i\omega r}{2K_{\text{air}}} + Z_{\text{rad}}^{-1} \right)^{-1}. \quad (29)$$

The radiative term  $Z_{\text{rad}}$  will generally lead to a mass-like drop in the low frequency limit Robey [16]. The frequency dependence of the stiffness term  $i\omega r/(2K_{\text{air}})$  leads to another drop in  $Z_{\text{gap}}$  at higher frequencies. If the liner surface input impedance is larger than  $Z_{\text{gap}}$ , the uncorrected characterisation result for this term is governed by the air gap instead of the specimen, which will be quantified in the following subsection. The power radiated through the rim of the gap towards the neighbouring patches leads to an overestimation of transfer terms. Experimental results confirming this behaviour will be presented in section 4.2. The affected frequency range depends on the liner type and the air-gap height  $h$ . A lower height naturally leads to a higher air-gap impedance and to improved characterisation results.

### 3.5.1. Experimental air gap correction

For an experimental correction procedure, the air gap is discretised into the patch grid defined on the specimen surface. Since the thickness of the air gap is very small as compared to the wavelength in the frequency range of interest, the pressure may be considered uniformly distributed within the air gap of each patch. The pressure vector  $\mathbf{p}^\beta$  measured at the top surface of the liner may now be approximated by

$$\mathbf{p}^\beta = \mathbf{Z}_{\text{gap}} (\mathbf{v}^\gamma - \mathbf{v}^\beta) \quad (30)$$

where  $\mathbf{v}^\gamma$  is the velocity vector containing the patch velocities measured with the particle velocity transducers at the upper surface of the air gap.  $\mathbf{Z}_{\text{gap}}$  represents the air gap impedance matrix. The desired patch velocity vector  $\mathbf{v}^\beta$  at the liner surface is obtained as

$$\mathbf{v}^\beta = \mathbf{v}^\gamma - \mathbf{Z}_{\text{gap}}^{-1} \mathbf{p}^\beta. \quad (31)$$

The air gap impedance matrix  $\mathbf{Z}_{\text{gap}}$  may be assessed experimentally beforehand by replacing the liner specimen with a rigid dummy ( $\mathbf{v}^\beta = 0$ ). By acquiring a sufficient number of independent load cases the air gap impedance  $\mathbf{Z}_{\text{gap}}$  can again be obtained through a matrix inversion. Thus the particle velocity at the liner specimen surface is reconstructed from the measurement with *PU* sensors at a finite distance from the specimen.

## 4. Characterisation results

In this section results of the experimental characterisation of a metal plate and a liner are presented. Surfaces are discretised into square patches of  $20 \times 20$  cm. Displayed levels for characterisation results are given in terms of impedance ( $L_Z = 20 \log_{10} \left| \frac{p}{v} \right|$ ) or mobility magnitudes ( $L_Y = 20 \log_{10} \left| \frac{v}{p} \right|$ ) with  $p$  in Pa and  $v$  in  $m/s$ , if not stated otherwise.

### 4.1. Plate characterisation

A clamped aluminium plate of dimensions  $1.7 \times 0.8$  m and a thickness of 5 mm (32 patches, Figure 5) has been characterised according to 3.1. A strip of 5 cm is neglected on two of the clamped edges, where the velocity amplitude in the considered frequency range is very low. Typical results for an input mobility  $Y_{11,11}$  (excitation and response on

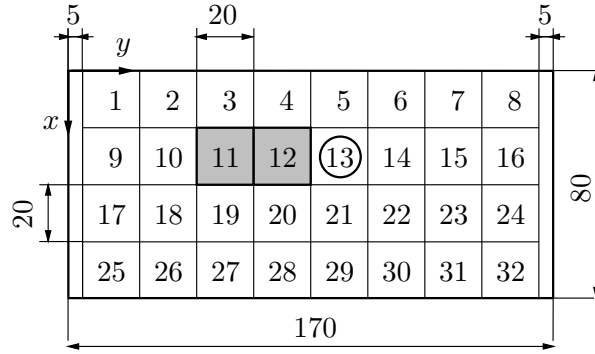


Figure 5: Patch grid on a clamped plate with neglected strips to the left and to the right (units: cm). The neighbouring patches 11 and 12 for which results are shown are marked in grey. Patch 13, where a point force is applied, is marked by a circle.

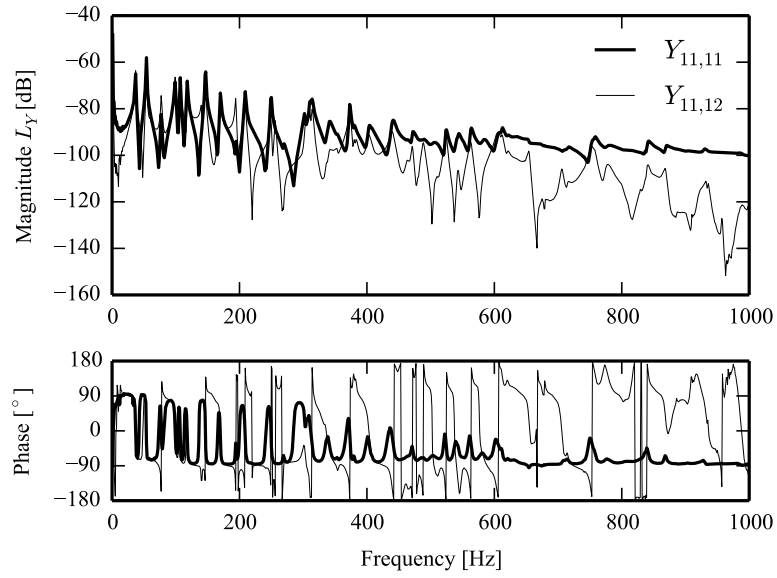


Figure 6: Example of components of the plate mobility matrix  $\mathbf{Y}$  – an input term  $Y_{11,11}$  and a transfer term  $Y_{11,12}$  to the neighbouring patch.

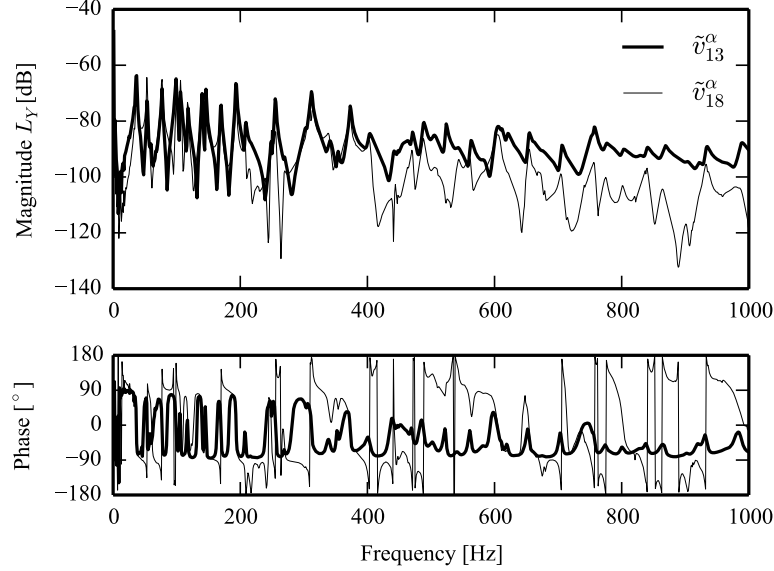


Figure 7: Example of components of the bare plate velocity vector  $\tilde{\mathbf{v}}^\alpha$  on patches 13 and 18. Here,  $L_Y = 20 \log_{10} \left| \frac{v}{F} \right|$  is the response to a force excitation of  $F = 1$  N at the centre of patch 13.

patch 11) and a transfer mobility  $Y_{11,12}$  (excitation on neighbouring patch 12) are shown in Figure 6.

For most of the lowest modes below 100 Hz, both amplitude and phase of  $Y_{11,11}$  and  $Y_{11,12}$  are similar. This is expected since the structural wavelength is much longer than the patch size in this frequency range. The average amplitude stays constant over frequency which is the typical behaviour for the driving-point mobility of thin plates [17]. In the region between 100 and 400 Hz the mobilities switch their phase relationship depending on the respective mode and a phase run-off due to propagating waves is visible in  $Y_{11,12}$ . Above 400 Hz resonance peaks of the input mobility  $Y_{11,11}$  are flattened increasingly, as the bending wavelength approaches twice the patch size (around 550 Hz).

In the high frequency range the patches are much larger than the structural wavelength and the averaged response of the plate due to uniformly distributed pressure excitation, that is, the wave mobility of the plate becomes mass governed [17], a feature which constitutes the basis for the well known mass-law for airborne sound transmissions of panels. The relative magnitude of the transfer mobility with respect to the input mobility decreases at higher frequencies.

Figure 7 shows an example of bare plate velocities  $\tilde{\mathbf{v}}^\alpha$  (source terms). The (internal) excitation consisted of a point force of 1 N at the centre of patch 13. In the high frequency range the source terms exhibit a more pronounced modal behaviour than the structural mobilities in Figure 6. This is due to the different types of excitation – uniform pressure for the structural mobilities and point force for the source terms.

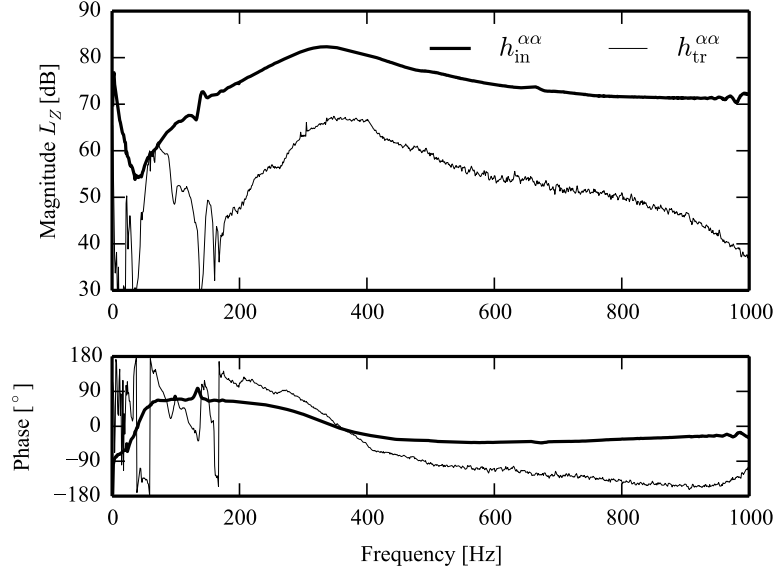


Figure 8: Bottom side input and transfer impedance with open top,  $\mathbf{h}^{\alpha\alpha}$ .

#### 4.2. Lining material characterisation

In this section some liner characterisation results are discussed. In this case the chosen liner consists of a typical automotive car floor trim package featuring three layers: a 7 mm moulded polyurethane foam of density  $85 \text{ kg/m}^3$  (structure side) covered by a  $2.2 \text{ kg/m}^2$  polymeric heavy layer topped by a 3 mm carpet (air cavity side).

##### 4.2.1. Bottom input/transfer impedance with open top, $\mathbf{h}^{\alpha\alpha}$

The sub-matrix  $\mathbf{h}^{\alpha\alpha}$  of  $\mathbf{H}$  contains input terms  $h_{\text{in}}^{\alpha\alpha} = h_{11}^{\alpha\alpha} = h_{22}^{\alpha\alpha}$  and transfer terms  $h_{\text{tr}}^{\alpha\alpha} = h_{12}^{\alpha\alpha} = h_{21}^{\alpha\alpha}$ . As pointed out in section (2.1) these terms can be interpreted as the input impedance at the bottom surface of the liner with pressure release conditions at its top surface. The reconstructed  $h_{\text{in}}^{\alpha\alpha}$  and  $h_{\text{tr}}^{\alpha\alpha}$  curves are shown in Figure 8.

Below  $f = 50 \text{ Hz}$  the stiffness of the whole system, due to excitation of a single patch and blocking the remaining patches, is visible in the input term  $h_{\text{in}}^{\alpha\alpha}$ . Between  $f = 50 \text{ Hz}$  and  $f = 300 \text{ Hz}$  the input term shows mass-governed behaviour, representing the mass of the full liner, that is, foam plus heavy layer plus carpet. At  $f \approx 335 \text{ Hz}$  the mass of the heavy layer including the carpet resonates on the stiffness of the foam layer. Above  $400 \text{ Hz}$  the heavy layer is decoupled and the amplitude of  $h_{\text{in}}^{\alpha\alpha}$  shows a stiffness-like decreasing trend with frequency. The contribution of  $h_{\text{tr}}^{\alpha\alpha}$  is most pronounced around the resonance. Below  $f = 100 \text{ Hz}$  transfer term measurements are not reliable due to structural vibration modes of the test rig and sensor noise.

##### 4.2.2. Cross/cross-transfer terms, $\mathbf{h}^{\alpha\beta}$ and $\mathbf{h}^{\beta\alpha}$

Cross terms  $\mathbf{h}^{\alpha\beta}$  and  $\mathbf{h}^{\beta\alpha}$  are plotted in Figure 9. Below  $f = 200 \text{ Hz}$  the two cross-input terms  $h_{\text{in}}^{\alpha\beta}$  and  $h_{\text{in}}^{\beta\alpha}$  are close to unity. For the case of  $h_{\text{in}}^{\beta\alpha}$  this means that a velocity



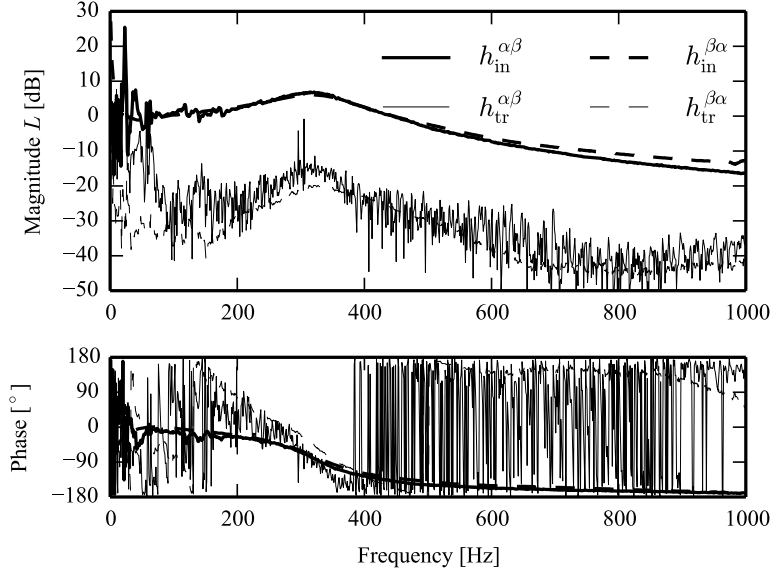


Figure 9: Cross terms  $h^{\alpha\beta}$  (speaker excitation above) and  $h^{\beta\alpha}$  (shaker excitation below).

excitation on  $\alpha$  would propagate to  $\beta$  with the same amplitude and phase if no pressure was exerted on  $\beta$ . The same holds for  $h_{in}^{\alpha\beta}$  with a propagation of pressure from  $\beta$  to  $\alpha$  with blocked surface  $\alpha$ . This is expected, as the specimen should behave like a rigid body below its eigenfrequencies. Errors due to structural modes of the test rig are clearly visible below  $f = 100$  Hz. Measurements of the pressure cross transfer term  $h_{tr}^{\alpha\beta}$  are limited by the signal-to-noise ratio. The terms show approximate reciprocity, but are not identical for at least two reasons: Firstly, reciprocity is only exactly valid for point transfer functions, but not necessarily for patches. Secondly, in the given set-up there is approximately a pressure-release condition on the top and a blocked condition on the bottom side. On the bottom side skeleton and fluid of the polyurethane foam are excited with the same velocity, whereas on the top side the fluid in the carpet layer is excited more efficiently by pressure than the stiffer and more massive skeleton (see section 3.3.2).

#### 4.2.3. Top input/transfer mobility with blocked bottom, $h^{\beta\beta}$

Figure 10 shows the top mobility of the sample<sup>1</sup>. Errors related to the air gap during the characterisation have been suppressed by the correction method described in section 3.5. The top mobility measurement is the only case where in addition to the resonance also the antiresonance of the heavy layer-carpet system is relevant. This antiresonance is visible at  $f \approx 550$  Hz and the behaviour follows a spring-mass-spring like curve: Below the resonance at  $f \approx 335$  Hz the foam stiffness governs the response. In the frequency range of  $f = 400 - 500$  Hz between resonance and antiresonance a mass-like behaviour

<sup>1</sup>Negative signs arise from the convention of positive velocities in the upwards direction, see section 2.1.

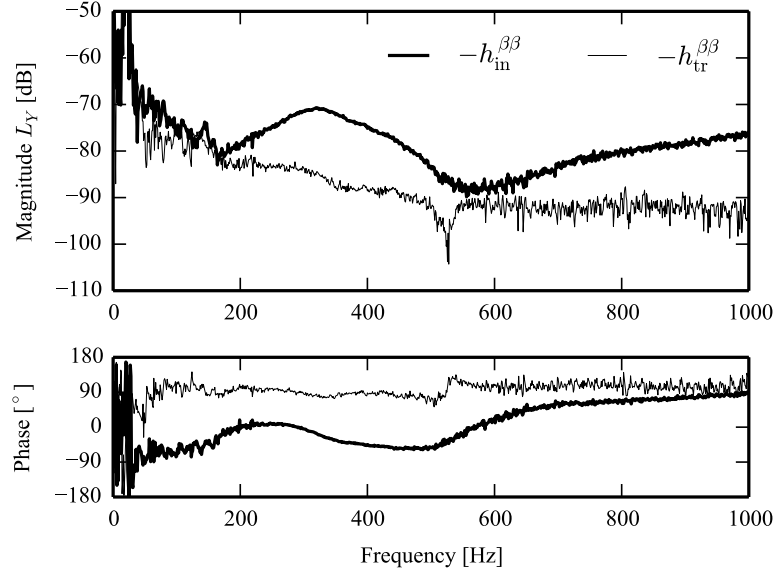


Figure 10: Top mobility with blocked bottom,  $h^{\beta\beta}$  with air gap correction applied.

of the decoupled mass of heavy-layer plus carpet is visible. Above the antiresonance, starting from  $f = 700$  Hz, the mobility is mainly governed by the carpet stiffness and damping. In this frequency range absorptive effects of the carpet layer start to become relevant for the cavity side. The accuracy of the results is limited by the air gap correction in both low and high frequency range, where the measured signal is determined mostly by the air gap impedance and not by the liner surface impedance.

#### 4.2.4. Air gap correction

Figure 11 shows results of measured air gap input and transfer impedances. *PU*-probes were placed 5 mm from the specimen surface for this measurement.

The air gap results indicate the behaviour described in 3.5: In the frequency range below 400 Hz the result is governed by the reactive part of the acoustic side wall radiation impedance. With rising frequency, the finite stiffness of the air gap becomes increasingly important. The correction eliminates the low-impedance gap masking the specimen surface mobility (Figure 12).

The correction of  $h_{in}^{\beta\beta}$  is significant across the whole frequency range. Especially in the stiffness dominated region below the first liner resonance the mass-governed leakage through the air gap edges is eliminated. The resonance of the heavy layer on the foam, while barely visible in the uncorrected case, is represented clearly in the corrected case. The transfer mobility  $h_{tr}^{\beta\beta}$  between the patches is reduced for all frequencies in the corrected version and remains significant around the anti-resonance at 550 Hz. The correction is limited by measurement noise. Accurate placement of the *PU* array is critical for the correction due to the strong particle velocity gradient near hard surfaces.

It should be noted, that the top surface could also be characterised with the interface

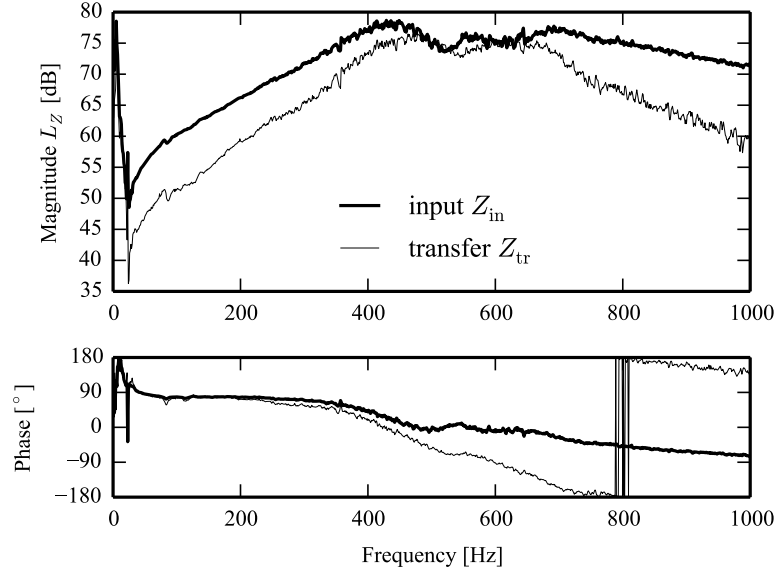


Figure 11: Air gap input and transfer impedance (liner specimen replaced by a rigid surface).

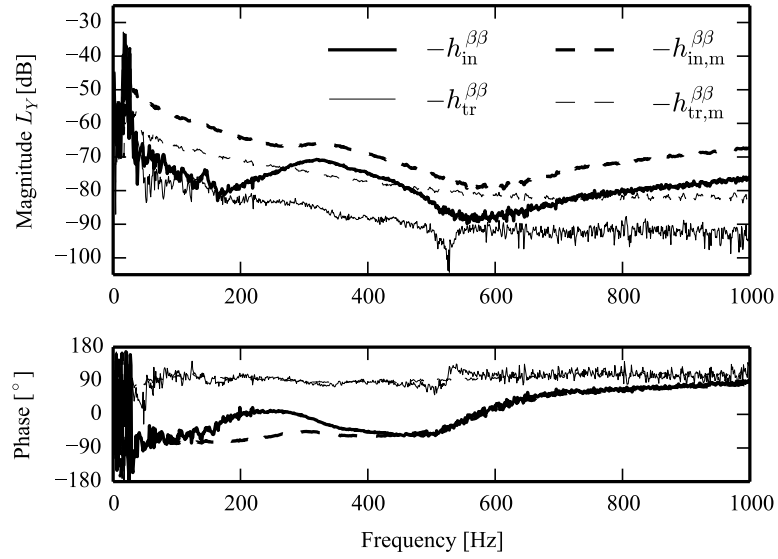


Figure 12: Comparison of corrected ( $h_{in}^{\beta\beta}$  and  $h_{tr}^{\beta\beta}$ ) and uncorrected ( $h_{in,m}^{\beta\beta}$  and  $h_{tr,m}^{\beta\beta}$ ) surface input and transfer mobilities.

defined on top of the air gap, that is, the air gap could be included in the liner. Consequently, no correction would be necessary. However, in this case further transfer terms would have to be characterised in order to account for propagation inside the air gap to more distant patches.

## 5. Results for a coupled system

An experimental case study for the described coupling method has been performed on a physically coupled plate-liner-cavity system (Figure 1) with patches of  $20 \times 20$  cm. The system consists of the 5 mm aluminium plate described in section 4.1, a close-to-rigid cavity of  $1.7 \times 0.8 \times 1.0$  m and a mass-spring type liner (14 mm polyurethane foam,  $\rho = 69 \text{ kg/m}^3$  and a  $3 \text{ kg/m}^2$  heavy layer). The liner was characterised by the described procedure with similar results to the ones for the liner with an additional carpet layer described in the previous section, which was not available during the validation measurements. It was nevertheless chosen to present characterisation results for the latter, since it shows a richer behaviour in the frequency range where the carpet acoustic absorption is relevant.

The analytical solution described in [9] has been applied to generate the cavity impedance matrix. Results of the investigations and an example for a detailed analysis of effects of the liner on the system are presented below. For validation measurements, sound pressure levels  $L_p = 20 \log_{10} |p/p_0|$  are normalised to  $p_0 = 20 \text{ } \mu\text{Pa}$ .

### 5.1. Expected interaction between structure, liner and cavity

To illustrate regions where most interaction of the liner with the adjacent structural and cavity domains occurs, representative examples of interacting surface input terms are displayed in terms of impedances in Figure 13.

From this picture most structure-liner interaction is expected at the liner mass-spring resonance and at lower frequencies. Above the sampling limit for the structure at  $f = 550$  Hz plate mode peaks are smeared out as mentioned in section 4.1, so the approach is not representative any more for coupling between structure and liner. The sampling limit for air is given by  $f = 850$  Hz. Strong interaction of the liner with the cavity is limited to the range around the liner mass-spring resonance of 300 Hz, since no absorptive layer was included in this case study. Without liner treatment plate and cavity could be considered as weakly coupled in this frequency range, since their surface input impedances are of different orders of magnitude.

### 5.2. Validation and comparison to the bare system

To assess the coupling procedure's accuracy and validity range, the sound pressure level at a reference position in the cavity due to a force excitation of  $F = 1 \text{ N}$  in the centre of patch 13 (Fig. 5) is compared to the reconstructed value in Figure 14.

Except for isolated spikes at frequencies between 150 Hz and 200 Hz the trend of the measured signal is captured by the reconstruction up to 500 Hz. While certain modes show a reasonable match in terms of amplitude and damping, differences up to 20 dB in the amplitude and large phase differences can be identified in several regions. The reason for the appearance of the spikes is most likely related to inaccuracies in the characterisation of the liner matrix elements  $\mathbf{h}^{\alpha\alpha}$  (similar to Figure 8) and/or the plate mobility

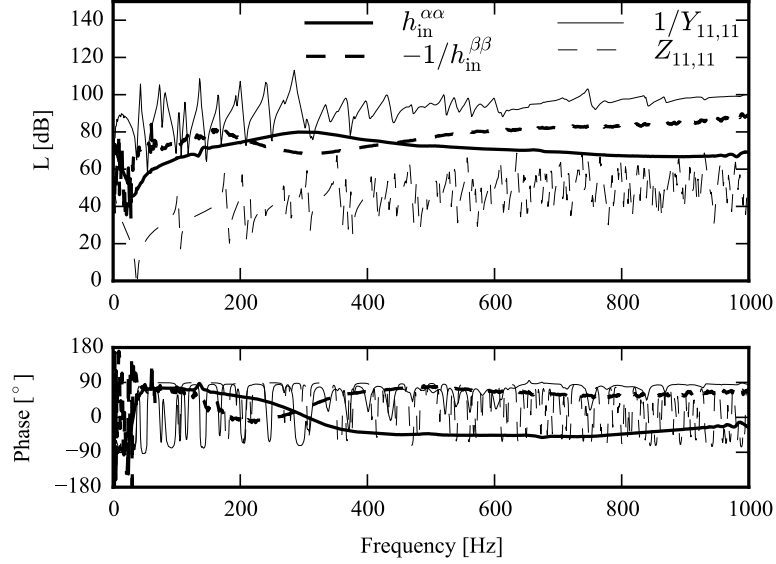


Figure 13: Comparison of impedance of structure, liner and cavity. The solid thin curve shows the inverse of a plate input mobility term,  $1/Y_{11,11}$ , the dashed thin curve a cavity input impedance term,  $Z_{11,11}$ . In-between, liner input impedances  $h_{in}^{\alpha\alpha}$  and  $-1/h_{in}^{\beta\beta}$  are displayed.

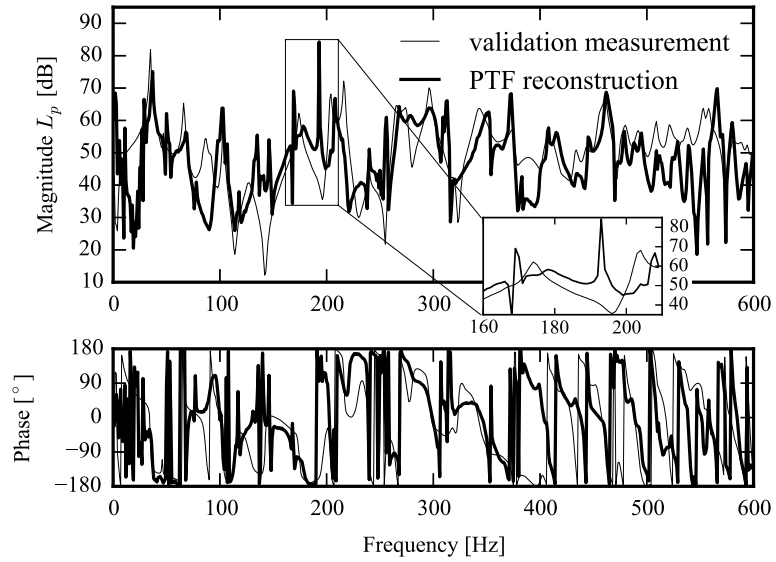


Figure 14: Comparison of measured and reconstructed sound pressure level at the reference microphone position in the cavity. A frequency region where the reconstruction shows spikes is shown in a detailed sub-plot.

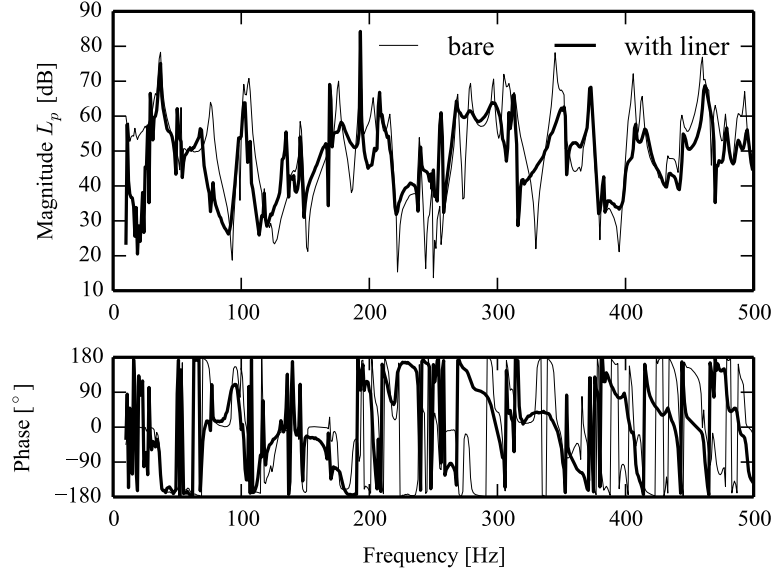


Figure 15: Reconstructed sound pressure level at the reference position, comparison to reconstruction of the bare system without liner.

matrix  $\mathbf{Y}$ . However, this topic requires further investigations. Above 500 Hz strong discrepancies between measurement and reconstruction appear which is in accordance with reaching the sampling limit for plate bending waves at 550 Hz.

Figure 15 shows a comparison of a reconstruction of the bare plate radiating into the cavity and the system response including the liner within the validity region.

Reduction in the sound pressure level is observed across the whole validity range, reaching more than 10 dB at and above the mass-spring resonance frequency. This is comparable to the reduction observed in direct measurements. In the region below the resonance plate modes are slightly shifted to lower frequencies due to additional mass loading.

### 5.3. Analysis of noise level reduction mechanisms

As mentioned in the introduction, inserting lining material reduces the sound pressure level inside the cavity by a combination of structural damping, transmission through the liner and cavity damping. The described coupling method is well suited to analyse the respective contributions from these different mechanisms. In order to study a certain aspect, the corresponding matrix element is kept and the remaining ones are fixed to artificially disable all other effects on the system. Figures 16-18 show the effect of the liner for the cases of only structural loading, transmission or cavity loading respectively.

Structural damping is dominant below and around the mass-spring resonance of the liner at 300 Hz (Figure 16). At frequencies above 450 Hz little damping is observed. Transmission through the liner is enhanced around the mass-spring resonance frequency and is reduced by decoupling at higher frequencies. In the overall result (Figure 15)

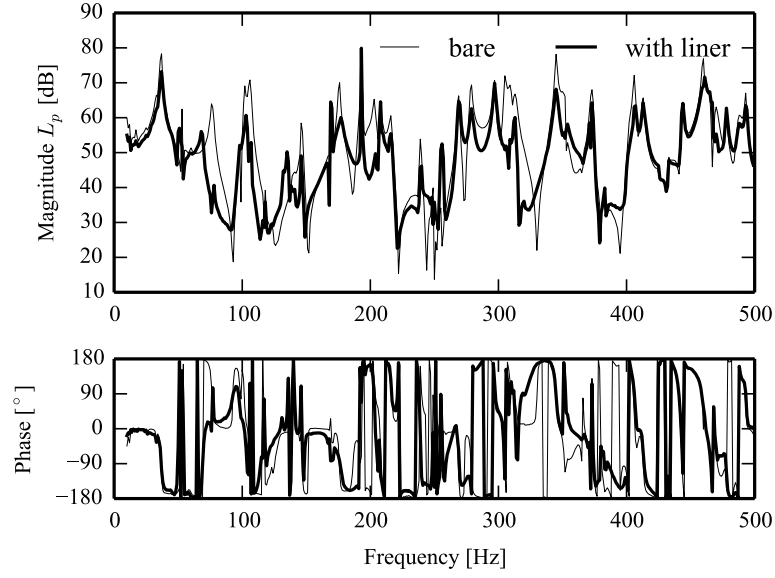


Figure 16: Reconstructed sound pressure level at reference position – considering only plate loading  $\mathbf{h}^{\alpha\alpha}$  ( $\mathbf{h}^{\alpha\beta} = \mathbf{h}^{\beta\alpha} = \mathbf{I}$ ,  $\mathbf{h}^{\beta\beta} = \mathbf{0}$ ).

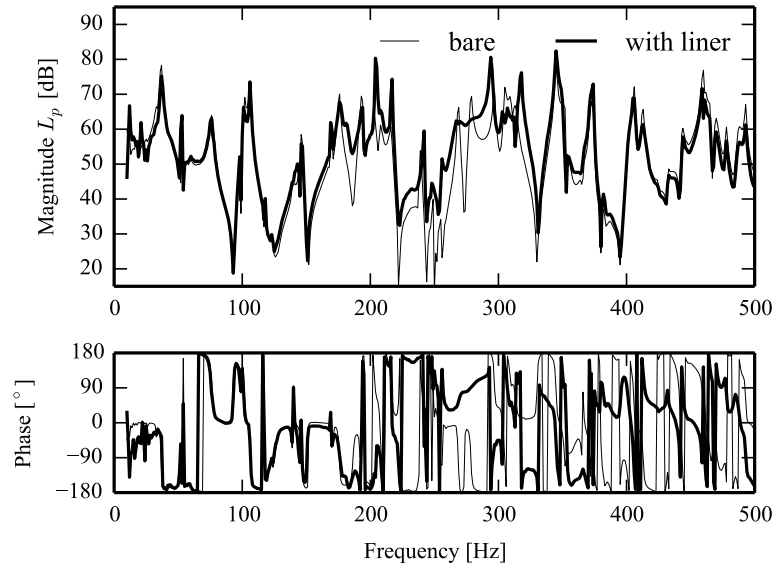


Figure 17: Reconstructed sound pressure level at reference position – considering only transmission  $\mathbf{h}^{\alpha\beta}$ ,  $\mathbf{h}^{\beta\alpha}$  ( $\mathbf{h}^{\alpha\alpha} = \mathbf{h}^{\beta\beta} = \mathbf{0}$ ).

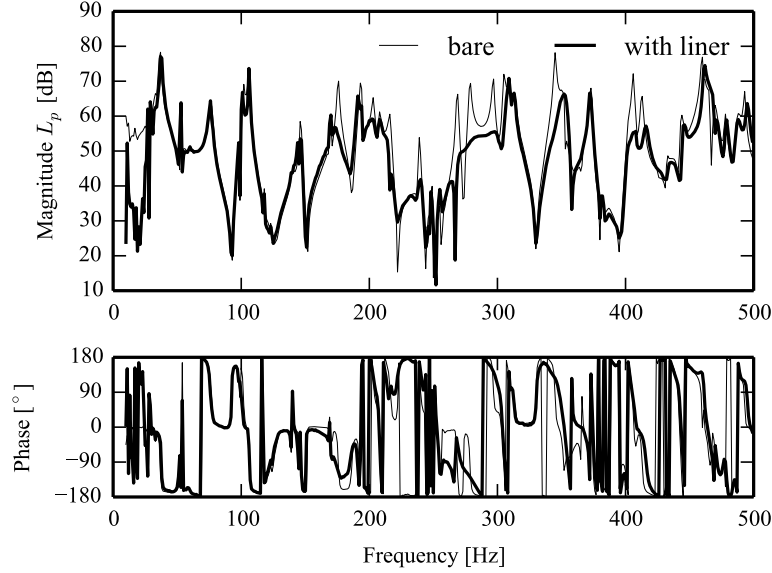


Figure 18: Reconstructed sound pressure level at the reference position – considering only cavity loading  $\mathbf{h}^{\beta\beta}$  ( $\mathbf{h}^{\alpha\alpha} = \mathbf{0}$ ,  $\mathbf{h}^{\alpha\beta} = \mathbf{h}^{\beta\alpha} = \mathbf{I}$ ).

this leads to a net increase of the cavity sound pressure level in some frequency zones between 200 Hz and 400 Hz. The remaining spikes in the reconstruction are considered to be artefacts as mentioned in the previous subsection. Cavity damping is realised mostly around the mass-spring resonance. This seems reasonable, since the surface of the heavy layer was airtight and should not act as a porous absorber.

## 6. Limitations and Outlook

The coupling approach by patch transfer functions and the presented characterisation methods are subject to several limitations that will be summarised here. Most importantly, spatial discretisation leads to an upper frequency limit caused by aliasing when the wavelength approaches twice the patch dimension. For strongly interacting systems the wavelength criterion is expected to be even stricter [8]. To extend the valid frequency range one needs to acquire transfer functions between a larger number of smaller patches. Once the direct experimental characterisation of the structure by the current method becomes too time-consuming (section 4.1), a numerical model would be preferred instead for this task. The same holds for the proposed experimental characterisation of fluid domains.

In the coupling between structure and liner, shear stresses are not considered explicitly (section 2.1). While this approximation is justified for certain systems, the explicit measurement of shear stresses may be required for liners that are strongly bonded to a structure.



As opposed to models based on material parameters, experimentally characterised patch transfer functions do not allow for later adjustments in material parameters or geometry. The assumption of rapid spatial decay of transfer functions in the liner (section 3.4) has to be verified for the respective specimen and patch dimension. For this purpose a test rig with a movable patch configuration would be advantageous. To obtain transfer functions to further patches one might consider the enhancement of characterisation data by Green's function methods [18]. A comparison to results from material models based on Biot parameters would be of great interest for cross-validation and to find possibilities to improve the liner characterisation method.

## 7. Concluding remarks

A prediction method for the vibro-acoustic response of a coupled system consisting of structure, lining material and fluid has been presented. A patch transfer function approach employing experimentally obtained subsystem characterisation data has been applied. Experimental methods have been described for a plate and a lining material with a heavy layer topped with a carpet. Results from liner measurements indicate, that for typical multi-layer materials, a reasonably accurate characterisation of input and next-neighbour terms at a length scale of 20 cm is possible in a frequency range of 100 – 1000 Hz. The accuracy is mainly limited by resonances in the test rig, the finite air gap and sensor signal-to-noise ratios. The predicted response of a plate-liner-cavity-system was compared to validation measurements performed on a physically coupled system. Input data for the reconstruction consisted of experimentally determined impedance matrices for structure and liner and an analytical model for an air cavity with hard walls. Reconstructed results are comparable to results from validation measurements in the expected validity region. As an application example, different aspects of lining material effects on the coupled response (structural damping, transmission, cavity damping) were analysed separately.

## Acknowledgements

The research work of Giorgio Veronesi has been funded by the European Commission within the ITN Marie Curie Action project GRESIMO under the 7th Framework Programme (EC grant agreement no. 290050). The authors acknowledge the financial support of the “COMET K2 – Competence Centres for Excellent Technologies Programme” of the Austrian Federal Ministry for Transport, Innovation and Technology (BMVIT), the Austrian Federal Ministry of Science, Research and Economy (BMWFW), the Austrian Research Promotion Agency (FFG), the Province of Styria and the Styrian Business Promotion Agency (SFG). Furthermore, the authors express their gratitude to the consortium partners BMW AG, IAC GmbH, Microflown Technologies, ESI GmbH and Université de Sherbrooke for their support. Finally, the authors gratefully acknowledge the support of COST action TU1105.

## References

- [1] A. Kropp, D. Heiserer, Efficient Broadband Vibro-Acoustic Analysis of Passenger Car Bodies Using an FE-Based Component Mode Synthesis Approach, *J. Comp. Acous.* 11 (02) (2003) 139–157, doi: 10.1142/s0218396x03001870.

- [2] M. Delany, E. Bazley, Acoustical properties of fibrous absorbent materials, *Applied Acoustics* 3 (2) (1970) 105–116, doi:10.1016/0003-682x(70)90031-9.
- [3] R. Lanoye, G. Vermeir, W. Lauriks, R. Kruse, V. Mellert, Measuring the free field acoustic impedance and absorption coefficient of sound absorbing materials with a combined particle velocity-pressure sensor, *J. Acoust. Soc. Am.* 119 (5) (2006) 2826, doi:10.1121/1.2188821.
- [4] N. Atalla, M. A. Hamdi, R. Panneton, Enhanced weak integral formulation for the mixed (u,p) poroelastic equations, *J. Acoust. Soc. Am.* 109 (6) (2001) 3065, doi:10.1121/1.1365423.
- [5] J. F. Allard, *Propagation of Sound in Porous Media*, Springer Netherlands, doi:10.1007/978-94-011-1866-8, 1993.
- [6] L. Jaouen, A. Renault, M. Deverge, Elastic and damping characterizations of acoustical porous materials: Available experimental methods and applications to a melamine foam, *Applied Acoustics* 69 (12) (2008) 1129–1140, doi:10.1016/j.apacoust.2007.11.008.
- [7] M. Ouisse, L. Maxit, C. Cacciolati, J.-L. Guyader, Patch Transfer Functions as a Tool to Couple Linear Acoustic Problems, *J. Vib. Acoust.* 127 (5) (2005) 458, doi:10.1115/1.2013302.
- [8] M. Aucejo, L. Maxit, N. Totaro, J.-L. Guyader, Convergence acceleration using the residual shape technique when solving structure–acoustic coupling with the Patch Transfer Functions method, *Computers & Structures* 88 (11-12) (2010) 728–736, doi:10.1016/j.compstruc.2010.02.010.
- [9] G. Pavić, Air-borne sound source characterization by patch impedance coupling approach, *Journal of Sound and Vibration* 329 (23) (2010) 4907–4921, doi:10.1016/j.jsv.2010.06.003.
- [10] J. Rejlek, G. Veronesi, C. Albert, E. Nijman, A. Bocquillet, A Combined Computational-Experimental Approach for Modelling of Coupled Vibro-Acoustic Problems, in: *SAE 2013 Noise and Vibration Conference and Exhibition*, SAE International, 2013–01–1997, doi:10.4271/2013-01-1997, SAE Technical Paper, 2013.
- [11] G. Veronesi, C. Albert, E. Nijman, J. Rejlek, A. Bocquillet, Patch Transfer Function Approach for Analysis of Coupled Vibro-Acoustic Problems Involving Porous Materials, in: *8th International Styrian Noise, Vibration & Harshness Congress*, SAE International, 2014–01–2092, doi:10.4271/2014-01-2092, SAE Technical Paper, 2014.
- [12] B. Petersson, B. Gibbs, Towards a structure-borne sound source characterization, *Applied Acoustics* 61 (3) (2000) 325–343, doi:10.1016/s0003-682x(00)00037-2.
- [13] Y. I. Bobrovitskii, A theorem on the representation of the field of forced vibrations of a composite elastic system, *Acoust. Phys.* 47 (5) (2001) 507–510, doi:10.1134/1.1403536.
- [14] J. Bolton, N.-M. Shiau, Y. Kang, Sound transmission through multi-panel structures lined with elastic porous materials., *Journal of Sound and Vibration* 191 (3) (1996) 317 – 347, ISSN 0022-460X, doi: <http://dx.doi.org/10.1006/jsvi.1996.0125>.
- [15] P. Debergue, R. Panneton, N. Atalla, Boundary conditions for the weak formulation of the mixed (u,p) poroelasticity problem, *The Journal of the Acoustical Society of America* 106 (5) (1999) 2383–2390, doi:<http://dx.doi.org/10.1121/1.428075>.
- [16] D. H. Robey, On the Radiation Impedance of an Array of Finite Cylinders, *J. Acoust. Soc. Am.* 27 (4) (1955) 706, doi:10.1121/1.1908001.
- [17] L. Cremer, M. Heckl, B. Petersson, *Structure-Borne Sound*, Springer Berlin Heidelberg, doi: 10.1007/b137728, 2005.
- [18] L. Alimonti, N. Atalla, A. Berry, F. Sgard, Assessment of a hybrid finite element-transfer matrix model for flat structures with homogeneous acoustic treatments, *J. Acoust. Soc. Am.* 135 (5) (2014) 2694–2705, doi:10.1121/1.4871355.